Wavevector and spin-flop transitions in cubic FeGe

1990 J. Phys.: Condens. Matter 2 7503

(http://iopscience.iop.org/0953-8984/2/36/013)

J. Phys.: Condens. Matter **2** (1990) 7503–7510. Printed in the UK

Wavevector and spin-flop transitions in cubic FeGe

M L Plumer

Centre de Recherche en Physique du Solide et Département de Physique, Université de Sherbrooke, Sherbrooke, Québec J1K 2R1, Canada

Received 30 October 1989, in final form 26 February 1990

Abstract. Recent neutron diffraction data showing unusual temperature and magnetic-field-induced magnetic reordering in the helical spin-density wave phase of cubic FeGe is analysed in terms of a Landau-type free energy previously used to study related phenomena in isostructural MnSi. The predicted magnetic phase diagrams (H–T) exhibit novel types of first-order and second-order wavevector and spin reorientation phase transitions.

MnSi and the cubic polymorph of FeGe are intermetallic compounds which exhibit the relatively rare phenomenon of a helical spin-density wave stabilised by the Dzyaloshinskii–Moriya interaction [1–3]. These materials have the tetrahedral $P2_13$ crystal structure where the lack of a centre of inversion symmetry is responsible for this type of antisymmetric exchange coupling. In MnSi, the Néel temperature is approximately 29 K with the spin density modulation characterised by a wavevector $\boldsymbol{Q}$ in a $\langle 111 \rangle$ direction and a long periodicity $Q \simeq 0.035$ Å^{-1} ($\lambda \simeq 180$ Å) [4]. There has been much experimental [4–6] and theoretical [3, 7–9] study of the magnetic ordering process of this compound under the influence of an applied magnetic field. For the case $\boldsymbol{H} \parallel \langle 111 \rangle$, the field induces a uniform moment $\boldsymbol{m} \parallel \boldsymbol{H}$ while reducing the amplitude of the spin polarisation vector $\boldsymbol{S}$ ($\perp \boldsymbol{Q}$), creating a conical spin structure. At sufficiently high field values $\boldsymbol{H}_c$, S is reduced to zero and a field-induced ferromagnetic (paramagnetic) phase is achieved. If the field is applied in other directions, $\boldsymbol{Q}$ first rotates towards the field direction (maintaining $\boldsymbol{S} \perp \boldsymbol{Q}$). For $\boldsymbol{H} \parallel \langle 100 \rangle$ or $\boldsymbol{H} \parallel \langle 110 \rangle$, there is an associated second-order wavevector and spin reorientation phase transition predicted to occur at the critical field $\boldsymbol{H}_{sr}$, where $\boldsymbol{Q} \parallel \boldsymbol{H}$ (i.e. $\boldsymbol{S} \perp \boldsymbol{H}$) for $\boldsymbol{H} > \boldsymbol{H}_{sr}$.

In contrast with naive expectation, recent neutron diffraction data [10] suggests that the magnetic ordering process of cubic FeGe is considerably more complicated than in the prototype compound MnSi. At temperatures not too far below $T_N \simeq 280$ K, the spin-density wave is described by a wavevector $\boldsymbol{Q}$ along a $\langle 100 \rangle$ direction with a very long periodicity $Q \simeq 0.009$ Å^{-1} ($\lambda \simeq 700$ Å). As the temperature is lowered, a 'sluggish' transition occurs at T_2 to a phase characterised by $\boldsymbol{Q}$ along a $\langle 111 \rangle$ axis, with little change in the wavelength. Large hysteresis is observed at this wavevector reorientation with $T_{2\downarrow} \simeq 211$ K and $T_{2\uparrow} \simeq 245$ K. The spin polarisation vector appears to remain in the configuration $\boldsymbol{S} \perp \boldsymbol{Q}$ at all $T < T_N$. The effect of a magentic field applied along a $\langle 110 \rangle$ direction at 250 and 140 K was observed to cause $\boldsymbol{Q}$ to rotate towards $\boldsymbol{H}$ (again with $\boldsymbol{S} \perp \boldsymbol{Q}$). At 250 K, $\boldsymbol{Q}$ remains along $\langle 100 \rangle$ for $\boldsymbol{H} \lesssim 0.08$ kOe and then rotates towards $\boldsymbol{H}$ with increasing field strength, where $\boldsymbol{Q} \parallel \boldsymbol{H}$ for $H \gtrsim 0.18$ kOe. At 140 K, $\boldsymbol{Q}$ slowly turns from a $\langle 111 \rangle$ axis towards $\boldsymbol{H}$ with increasing field, with $\boldsymbol{Q} \parallel \boldsymbol{H}$ for $H \gtrsim 0.40$ kOe. Qualitatively different behaviour for the field dependence of $\boldsymbol{Q}$ between these two tem-

0953-8984/90/367503 + 08 $03.50

peratures is thus seen. Neutron diffraction data on the magnetic ordering process with $\boldsymbol{H}$ along other directions have not been reported.

In this work, a Landau-type free energy previously used to model the wavevector and spin reorientation in MnSi is analysed in a effort to understand further the data in [10] for FeGe. By simply changing the sign of a certain coefficient in the free energy (relative to its sign used for MnSi), which is related to magnetic dipole–dipole interactions, qualitative agreement with the results outlined above is obtained. A first-order wavevector and spin-flop transition is predicted to occur at T_2 from the high-T phase with $\boldsymbol{Q} \parallel \langle 100 \rangle$ to the low-T phase with $\boldsymbol{Q} \parallel \langle 111 \rangle$. For $\boldsymbol{H} \parallel \langle 110 \rangle$, the wavevector and spin reorientation phase transition H_{sr} is predicted to be second order for $T < T_2$ and first-order for $T > T_2$. Numeric and analytic results for the predicted magnetic phase diagrams with $\boldsymbol{H}$ along $\langle 100 \rangle$ and $\langle 111 \rangle$ are also presented.

The free energy used in [7] (hereafter referred to as I) to study the wavevector and spin reorientation in MnSi is written in terms of variables describing the long-range magnetic order (spin density averaged over a unit cell) given by

$$\boldsymbol{s}(\boldsymbol{r}) = \boldsymbol{m} + \boldsymbol{S}\, e^{i\boldsymbol{Q}\cdot\boldsymbol{r}} + \boldsymbol{S}^* e^{-i\boldsymbol{Q}\cdot\boldsymbol{r}}. \tag{1}$$

Here, $\boldsymbol{S}$ is the (complex) spin polarisation vector written as $\boldsymbol{S} = \boldsymbol{S}_1 + i\boldsymbol{S}_2$ where $\boldsymbol{S}_1$ and $\boldsymbol{S}_2$ are real vectors. The helical spin configuration is described by taking $\boldsymbol{S}_1 \perp \boldsymbol{S}_2 \perp \boldsymbol{Q}$ with $S_1^2 = S_2^2 = \frac{1}{2}S^2$. Using these relations, the free energy, expanded to fourth order in $\boldsymbol{s}$ and constructed so as to be invariant with respect to the symmetry operations of the space group, can be simplified to the following form (see equation (2.4) of I):

$$F = \tfrac{1}{2}A_0 m^2 + A_Q S^2 + Bm^2 S^2 + BS^4 + \tfrac{1}{4}Bm^4 + B' m_\perp^2 S^2 + (\tfrac{1}{2}DQ^2 S^2 + \tfrac{1}{4}ES^4)g - m_\parallel H \cos\theta - m_\perp H \sin\theta \tag{2}$$

$$g = 1 + \beta_1^4 + \beta_2^4 + \beta_3^4 \tag{3}$$

where β_1, β_2 and β_3 are the direction cosines of $\boldsymbol{Q}$ relative to the crystallographic axes; θ is the angle between $\boldsymbol{Q}$ and $\boldsymbol{H}$; $m_\parallel$ and $m_\perp$ are the components of $\boldsymbol{m}$ parallel and perpendicular to $\boldsymbol{Q}$, respectively. Temperature dependence is assumed to enter in the usual way by writing

$$A_0 = a(T - T_0) \qquad A_Q = a(T - T_Q) \tag{4}$$

where $T_0 \lesssim T_Q$ since Q is small. In the present work it is assumed that $B' \simeq B$, which can be shown to be good approximation for systems with small Q [11]. As discussed in I, the anisotropy coefficients D and E are expected to be much smaller than corresponding coefficients of isotropic terms, e.g. $E \ll B$ and $DQ^2 \ll \Delta$, where $\Delta \equiv A_0 - A_Q = a(T_Q - T_0)$. The Dzyaloshinskii–Moriya term of the form $F_c = 2C\boldsymbol{Q} \cdot (\boldsymbol{S}_1 \times \boldsymbol{S}_2)$ is hidden in the coefficient A_Q and details of how this interaction stabilises long-wavelength helical spin structures can be found in I. Note that renormalisation group arguments [2] suggest that the transition at T_N in these types of system is driven to be weakly first order by critical fluctuations. Within the present mean-field analysis, this transition is predicted to be second order.

In the absence of an applied magnetic field, the direction of $\boldsymbol{Q}$ is determined by the anisotropy energy $F_A = E_A g$, where

$$E_A = dS^2 + \tfrac{1}{4}ES^4 \tag{5}$$

with $d \equiv \frac{1}{2}DQ^2$ and $S^2 \sim T_N - T$. For $E_A > 0$, $\boldsymbol{Q}$ is stabilised along a $\langle 111 \rangle$ axis whereas, for $E_A < 0$, $\boldsymbol{Q}$ lies along a $\langle 100 \rangle$ direction. The experimental results for MnSi are accounted for by assuming that $E_A > 0$, and further that $d > 0$, and $E > 0$. A model to

describe the data for FeGe can be made by assuming that $d < 0$ and $E > 0$. In this way it is seen that $E_A < 0$ at temperatures close to T_N where S^2 is small. At lower temperatures, E_A can change sign if the E-term in (5) becomes dominant. This model provides a mechanism for a first-order phase transition at some temperature T_2 from a high-T state with $\boldsymbol{Q} \parallel \langle 100 \rangle$ to a low-T state with $\boldsymbol{Q} \parallel \langle 111 \rangle$ (also see [3] and [12]).

With a magnetic field present, there can be competition between the anisotropy E_A and the terms $B' m_\perp^2 S^2 - \boldsymbol{m} \cdot \boldsymbol{H}$. The latter terms are minimised by a configuration with $m_\perp = 0$ (since $B' = B > 0$) and $\theta = 0$, i.e. $\boldsymbol{Q} \parallel \boldsymbol{H}$.

Expressions for the two zero-field transition temperatures can be obtained from (2) in the following way. The Néel temperature is determined by setting the coefficient of S^2 equal to zero. With $\boldsymbol{Q} \parallel \langle 100 \rangle$, this gives

$$T_N = T_Q - 2d/a. \tag{6}$$

The first-order wavevector and spin-flop transition temperature T_2 can be obtained by equating the free energies corresponding to $\boldsymbol{Q} \parallel \langle 100 \rangle$ and $\boldsymbol{Q} \parallel \langle 111 \rangle$, with S^2 satisfying the relation $\partial F / \partial S^2 = 0$ in each case. Using the approximation $E \ll B$, this procedure yields

$$T_2 \simeq T_N + 8d/a(E/B). \tag{7}$$

This approximate result also corresponds to the temperature at which $E_A = 0$. Note that, since both d and E/B are small quantities, their ratio need not be small so that T_2 can be well below T_N.

Crude estimates for some of the parameter values, for the purpose of numerical work, can be obtained in the following way. For a magnetic field applied along one of the three principal crystallographic axes $\langle 100 \rangle$, $\langle 110 \rangle$ or $\langle 111 \rangle$, the configuration $\boldsymbol{Q} \parallel \boldsymbol{H}$ is achieved at sufficiently high field values and at temperatures not too close to T_N (see I and below). It is then straightforward to determine the critical field $\boldsymbol{H}_c$ above which $S = 0$:

$$\boldsymbol{H}_c = m_c(\Delta - dg) \tag{8}$$

$$m_c^2 = (-A_N + 2d - dg)/B \tag{9}$$

where $A_N = a(T - T_N)$ with $g = 2, \frac{3}{2}$ and $\frac{4}{3}$ for $\boldsymbol{H}$ along $\langle 100 \rangle$, $\langle 110 \rangle$ and $\langle 111 \rangle$, respectively. Since $d < 0$, these results can be used to predict that, at low temperatures (where $|A_N| \ll |d|$), $H_c^{\langle 100 \rangle} > H_c^{\langle 110 \rangle} > H_c^{\langle 111 \rangle}$, in agreement with values for $\boldsymbol{H}_c$ which can be extracted from the magnetisation data at 77 K in [13]. Estimates for some of the parameter values can then be obtained by comparing the relations (8) and (9) with these data: $d \simeq -0.27$, $\Delta \simeq 5.3$ and $B/a \simeq 1.7 \times 10^{-3}$ (in cgs units with m given in gauss). These values are not expected to be very reliable since truncation of the free energy at fourth order becomes a poor approximation at low temperatures. In addition, some fourth-order anisotropy terms which would be relevant for a complete quantitative analysis have been omitted from the free energy (2) (see I). For convenience we set $a = 1$, which is probably reasonable since $a = \Delta/(T_Q - T_0)$ and $T_0 \leqslant T_Q \leqslant T_N = 280$ K. Taking $T_2 = 228$ K as the mean of $T_{2\downarrow}$ and $T_{2\uparrow}$, the relation (7) can then be used for the estimate $E \simeq 6.8 \times 10^{-5}$. These estimates for the parameters are consistent with previously made remarks concerning their relative values.

For the calculated results presented below, $\boldsymbol{H}$ and $\boldsymbol{Q}$ are assumed to lie in the $(1\bar{1}0)$ plane, with $\boldsymbol{S} \perp \boldsymbol{Q}$. Walker [14] has recently shown in the case of MnSi that $\boldsymbol{Q}$ need not be confined to the $(1\bar{1}0)$ plane because of the small spin–orbit coupling terms D_1 and D_2 in the free energy (2.2) of I. As a consequence, there can be two successive phase transitions associated with the wavevector reorientation. The neutron diffraction data suggest that these effects are too small to be observed in the case of FeGe [10] and are omitted from the present calculation.

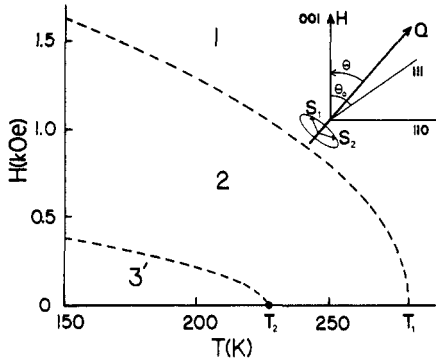

Figure 1. Numerically determined phase diagram with $\boldsymbol{H} \parallel [001]$ showing the paramagnetic phase (1), conical phase (2) with $\theta = 0$, $\boldsymbol{Q} \parallel [001]$ and ordered state (3′) with $0 < \theta < \theta_0$. The broken curves represent second-order transitions H_{sr} (3′–2) and H_c (2–1).

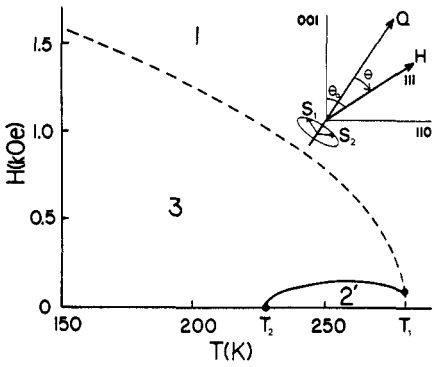

Figure 2. Phase diagram with $\boldsymbol{H} \parallel [111]$ showing the paramagnetic phase (1), conical phase (3) with $\theta = 0$, $\boldsymbol{Q} \parallel [111]$ and ordered state (2′) with $0 < \theta < \theta_0$. The broken curve represents the second-order transition H_c and the full curve denotes the first-order transition $\tilde{H}_{sr}$.

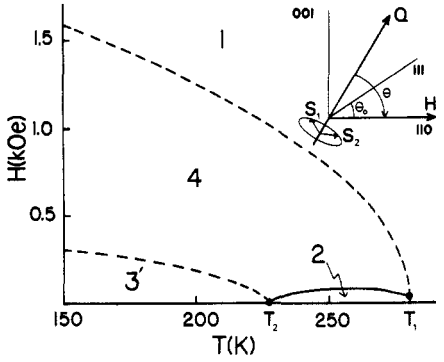

Figure 3. Phase diagram for $\boldsymbol{H} \parallel [110]$ showing the paramagnetic phase (1), conical phase (4) with $\theta = 0$, $\boldsymbol{Q} \parallel [110]$ and ordered states (3′) with $0 < \theta < \theta_0$ and (2) with $\theta = \pi/2$. The broken curves represent the second-order transitions H_c (1–4) and H_{sr} (3′–4) and the full curve denotes the first-order transition $\tilde{H}_{sr}$.

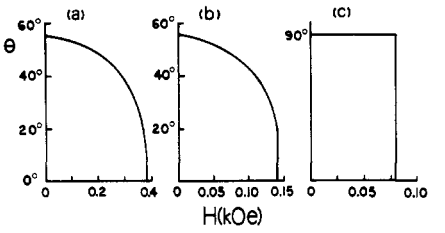

Figure 4. Field dependence of the angle θ between $\boldsymbol{Q}$ and $\boldsymbol{H}$ for (*a*) $\boldsymbol{H} \parallel [001]$ at $T = 150$ K, (*b*) $\boldsymbol{H} \parallel [111]$ at $T = 250$ K and (*c*) $\boldsymbol{H} \parallel [110]$ at $T = 250$ K.

Results of numerical minimisation of the free energy $F(S, m_{\parallel}, m_{\perp}, \theta)$ (equation (2)) for the magnetic phase diagrams corresponding to $\boldsymbol{H}$ along each of the three principal crystallographic axes are shown in figures 1–3. The analytically predicted first-order wavevector and spin-flop transition at T_2 in zero field (full circle at 228 K) from a state with $\boldsymbol{Q} \parallel [001]$ (phase 2: $T_2 < T < T_N$) to a state with $\boldsymbol{Q} \parallel [111]$ (phase 3: $T < T_2$) is confirmed. The paramagnetic state ($T > T_N$) is labelled as phase 1 in each figure, with second-order transitions represented by broken curves and first-order transitions by full curves. For $\boldsymbol{H} \parallel [001]$ (figure 1) and $T < T_2$, $\boldsymbol{Q}$ rotates from the [111] axis towards $\boldsymbol{H}$ with increasing field strength (phase 3′), where the 2–3′ phase boundary represents the second-order reorientation phase transition $\boldsymbol{H}_{sr}$, above which $\boldsymbol{Q} \parallel [001]$ ($\theta = 0$). An example of the field dependence of θ at 150 K is shown in figure 4(*a*). Phase 2 labels the

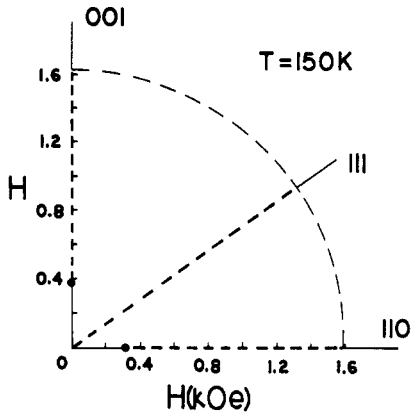

Figure 5. Phase diagram for $\boldsymbol{H}$ in the $(1\bar{1}0)$ plane at $T = 150$ K (see figures 1–3). The paramagnetic state (phase 1) is to the right of the (thin) broken curve. Lines of second-order transitions at which $\theta = 0$ ($\boldsymbol{Q} \| \boldsymbol{H}$) are indicated by the (heavy) broken lines along the three high-symmetry axes. $\theta > 0$ in all other regions of the diagram, including the ⟨001⟩ axis for $H < 0.39$ kOe and the ⟨110⟩ axis for $H < 0.31$ kOe.

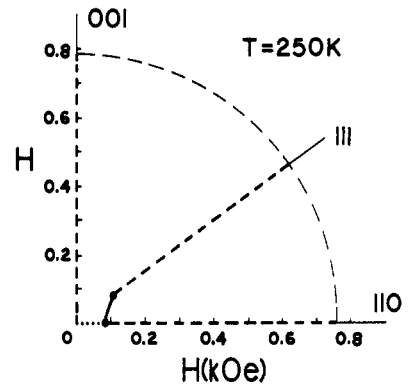

Figure 6. Phase diagram as in figure 5 for $T = 250$ K. The heavy full curve denotes a line of first-order transitions between two states with $\theta > 0$. The dotted portion of the ⟨110⟩ axis ($H < 0.09$ kOe) indicates $\theta = \pi/2$ ($\boldsymbol{Q} \| \langle 001 \rangle$).

conical spin structure, with $S \to 0$ at the 2–1 phase boundary $\boldsymbol{H}_c$. For $\boldsymbol{H} \| [111]$ (figure 2) and $T > T_2$, $\boldsymbol{Q}$ rotates from the [001] axis towards $\boldsymbol{H}$ at small field strengths (phase 2′) but then undergoes a first-order flop transition at $\tilde{\boldsymbol{H}}_{sr}$ to a state with $\boldsymbol{Q} \| [111]$ (phase 3). An example of the field dependence of θ at 250 K is given in figure 4(*b*). For $\boldsymbol{H} \| [110]$ (figure 3) and $T < T_2$, $\boldsymbol{Q}$ rotates from the [111] axis towards $\boldsymbol{H}$ (phase 3′) with a second-order transition at $\boldsymbol{H}_{sr}$ to a state with $\boldsymbol{Q} \| [110]$ (phase 4). At temperatures $T_2 < T < T_N$, $\boldsymbol{Q}$ remains along the [001] axis with increasing field strength (phase 2) until a critical value $\tilde{\boldsymbol{H}}_{sr}$ where a first-order flop transition occurs to phase 4; the field dependence of θ at 250 K is shown in figure 4(*c*). Note that $T = T_2$, $H = 0$ for figures 1 and 3 represents a point where a line of second-order transitions terminates at a first-order transition.

With the magnetic field applied in a direction other than one of the three high-symmetry axes, a configuration with $\boldsymbol{Q} \| \boldsymbol{H}$ is never achieved. This is illustrated in figures 5 and 6 which show portions of the phase diagram for $\boldsymbol{H}$ in the $(1\bar{1}0)$ plane at $T = 150$ K and 250 K, respectively.

Some approximate analytic expressions for the critical fields $\boldsymbol{H}_{sr}$ and $\tilde{\boldsymbol{H}}_{sr}$ can be derived following the analysis of section 3 in I. The results given below are valid over a wider range of temperature and anisotropy strengths than are the corresponding expressions reported in I. The extended results for $\boldsymbol{m}$, valid to first order in H, are

$$m_\parallel = \chi_\parallel H \cos\theta \qquad m_\perp = \chi_\perp H \sin\theta \tag{10}$$

with

$$\chi_\parallel \simeq (\Delta - rg)^{-1} \qquad \chi_\perp \simeq (\Delta - A_Q - 2rg)^{-1} \tag{11}$$

where $r = d + \frac{1}{2}ES_0^2$ and $S_0^2 = -A_Q/2B \simeq -A_N/2B$. Using these results together with the equilibrium expression for S^2, the free energy $F(\theta, H)$ valid to order H^2 can be written as (also see (3.7) of I)

$$F = F_0 + E_A g - \tfrac{1}{2}\chi_\parallel H^2 + \tfrac{1}{2}(\chi_\parallel - \chi_\perp)H^2 \sin^2\theta \tag{12}$$

where $E_A \simeq dS_0^2 + \frac{1}{4}ES_0^4$. The principal difference between the above results and those

of I is that here $\chi_\parallel$ and $\chi_\perp$ are dependent on the direction of $\boldsymbol{Q}$, i.e. θ dependent, through the function g. Results are given below taking $\boldsymbol{Q}$ and $\boldsymbol{H}$ to lie in the $(1\bar{1}0)$ plane with θ as defined in figures 1–3. After expanding the free energy to low order in $\sin\theta$, second-order transitions are determined by setting the coefficient of $\sin^2\theta$ equal to zero, and first-order transitions by directly comparing the free energies of the two relevant phases.

For $\boldsymbol{H} \parallel [001]$, the second-order reorientation transition corresponding with the 3′–2 phase boundary of figure 1 can be expressed as

$$H_{sr}^2 \simeq 4E_A/[\chi_\parallel^0(1 + 2r\chi_\parallel^0) - \chi_\perp^0] \tag{13}$$

where $\chi_\parallel^0$ and $\chi_\perp^0$ are determined from (11) by setting $g = 2$ ($\theta = 0$). For $\boldsymbol{H} \parallel [110]$, the 3′–4 phase boundary of figure 3 has a similar form (note factors of 2)

$$H_{sr}^2 \simeq 2E_A/[\chi_\parallel^0(1 + r\chi_\parallel^0) - \chi_\perp^0]. \tag{14}$$

where, here, $\chi_\parallel^0$ and $\chi_\perp^0$ are given by (11) with $g = \frac{3}{2}$. These results (13) and (14) are to be compared with (3.9) and (3.13), respectively, of I. An expression for the first-order 2–4 phase boundary of figure 3 for $\boldsymbol{H} \parallel [110]$ is

$$\tilde{H}_{sr}^2 \simeq -E_A/(\chi_\parallel^{(4)} - \chi_\perp^{(2)}) \tag{15}$$

where, from (11), $\chi_\parallel^{(4)} = \chi_\parallel(g = \frac{3}{2})$ and $\chi_\perp^{(2)} = \chi_\perp(g = 2)$. The multicritical point at the paramagnetic phase boundary where H_{sr} and H_c meet (see figure 3) is determined from (15) to occur at the critical field

$$\tilde{H}_{sr:C}^2 \simeq -d\Delta^2/2B. \tag{16}$$

The case of $\boldsymbol{H} \parallel [111]$ is somewhat special. An expansion of the free energy in powers of $\sin\theta$ reveals that there are odd-order terms, e.g. $\sin^3\theta$, which arise from the function g. Phase transitions involving θ are thus necessarily of first order, as confirmed numerically. The 2′–3 phase boundary of figure 2 can be expressed as

$$\tilde{H}_{sr}^2 \simeq -\tfrac{64}{21}E_A/[\chi_\parallel^0(1 - \tfrac{4}{3}r\chi_\parallel^0) - \chi_\perp^0] \tag{17}$$

where $\chi_\parallel^0$ and $\chi_\perp^0$ are given by (11) with $g = \frac{4}{3}$. In this case, the multicritical point at the paramagnetic phase boundary occurs at the critical field

$$\tilde{H}_{sr:C}^2 \simeq -32d\Delta^2/21B. \tag{18}$$

Note that the critical fields H_{sr} and $\tilde{H}_{sr}$ given above are zero at the temperature T_2 where $E_A = 0$, as required. Inserting the estimated parameter values into the above expressions (13)–(18) show that there is good agreement with the results of direct numerical minimisation of the free energy (and that the approximate expressions (3.9) and (3.13) of I are not very accurate in this case).

It is of interest to note that weak scattering at the harmonic wavevector $2\boldsymbol{Q}$ observed at 250 K with $\boldsymbol{H} \parallel \langle 110 \rangle$ and low field values (see figure 9 of [10]) is consistent with earlier predictions of a second harmonic [8], with an associated spin polarisation vector

$$\boldsymbol{S}_{2Q} = -(2B/A_{2Q})\boldsymbol{S}(\boldsymbol{m} \cdot \boldsymbol{S}). \tag{19}$$

Note that $\boldsymbol{S}_{2Q} = 0$ at $H = 0$ and also if $\boldsymbol{Q} \parallel \boldsymbol{H}$ (since, then, $\boldsymbol{m} \perp \boldsymbol{S}$); however, $\boldsymbol{S}_{2Q}$ is non-zero in the regions of phase 2 (as observed) and phase 3′ of figure 3, as well as phase 3′ of figure 1 and phase 2′ of figure 2. The disappearance of $\boldsymbol{S}_{2Q}$ at $\theta = 0$ is another signature of the second-order spin reorientation phase transitions.

Spin reorientation phase transitions are of the order–order (displacive) type, which contrast with the more familiar order–disorder kind (exemplified here by the paramagnetic phase boundary in figures 1–3, 5 and 6). Spin rotation has been much studied

in the rare-earth orthoferrites [15–17], which often involves a temperature-induced reorientation of the magnetisation vector from one crystallographic axis to another and is associated with two second-order phase transitions. In the case of field-induced spin rotation, second-order phase transitions are found to occur only for $\boldsymbol{H}$ applied along a high-symmetry axis, a feature also found in the present study.

Second-order phase transitions of this kind are in some ways weaker than those of the order–disorder type. Specific heat anomalies are small and the associated universality classes cannot be characterised simply by the space and spin dimensionality. Small anisotropy effects [18] or changes in crystal symmetry (through magnetoelastic coupling [8, 16, 19]) are usually involved. The effects of critical fluctuations (not accounted for in the present mean-field treatment) at the reorientation phase transitions are expected to be negligible owing to a linear coupling between the order parameter and shear strains [8, 12], giving rise to a critical dimensionality of 2.5 [16, 17].

It is then not surprising, for example, that, although the multicritical points of figure 2 where phases 1, 2′ and 3 meet, and of figure 3 where phases 1, 2 and 4 meet, have the apparent structure of the common bicritical point, they are not of that type. A bicritical point involves an order–disorder spin-flop transition between states of spin dimensionality n and $n-1$ [20], causing a significant distortion of the paramagnetic phase boundary (not present here), even within a Landau-type mean-field treatment [21]. The multicritical points of figures 2 and 3 do not involve a change in spin dimensionality but instead a somewhat less dramatic reorientation in the spin structure with respect to the crystallographic axes.

In conclusion, this work has demonstrated that, if the anisotropy coefficient D in the free energy (2) is negative, more complex temperature- and magnetic-field-induced wavevector and spin reorientation phenomena occur than in the previously analysed case of $D > 0$, which was appropriate for a description of MnSi. (The structure of the original form of this term (see (2.2) of [7]) is similar to that of the magnetic dipole–dipole interaction [11].) The results presented here provide a qualitative description of recent neutron diffraction data on cubic FeGe [10]. The large hysteresis and sluggish character observed at the zero-field transition T_2, from the high-T phase with $\boldsymbol{Q} \parallel \langle 100 \rangle$ to the low-T phase where $\boldsymbol{Q} \parallel \langle 111 \rangle$, is attributed to metastability and domain effects (not accounted for here) associated with the predicted first-order nature of this transition. The field-induced wavevector and spin reorientation observed with $\boldsymbol{H} \parallel \langle 110 \rangle$ at 140 K and at 250 K are predicted to be associated with second- and first-order phase transitions, respectively. Although numerical estimates of the model parameters based on earlier magnetisation data [13] are very crude, the resulting critical field values at these two temperatures (see figure 3), $H_{sr} \simeq 0.34$ kOe and $\tilde{H}_{sr} \simeq 0.08$ kOe, respectively, agree reasonably well with those extracted from the recent data [10]. The predicted magnetic phase diagrams of figures 1–3 should serve as useful guides for further experimental investigation of this novel magnetic reordering in the helical spin-density wave phase of cubic FeGe.

Acknowledgment

This work was supported by Natural Science and Engineering Research Council of Canada and FCAR du Québec.

References

[1] Nakanishi O, Yanase A, Hasegawa A and Kataoka M 1980 *Solid State Commun.* **35** 995
[2] Bak P and Jensen M H 1980 *J. Phys. C: Solid State Phys.* **13** L881

[3] Kataoka M and Nakanishi O 1981 *J. Phys. Soc. Japan* **50** 3888
[4] Ishikawa Y, Tajima K, Bloch D and Roth M 1976 *Solid State Commun.* **19** 525
[5] Kadowaki K, Okuda K and Date M 1982 *J. Phys. Soc. Japan* **51** 2433
[6] Ishikawa Y and Arai M 1984 *J. Phys. Soc. Japan* **53** 2726
[7] Plumer M L and Walker M B 1981 *J. Phys. C: Solid State Phys.* **14** 4689
[8] Plumer M L and Walker M B 1982 *J. Phys. C: Solid State Phys.* **15** 7181
[9] Plumer M L 1984 *J. Phys. C: Solid State Phys.* **17** 4663
[10] Lebech B, Bernhard J and Freltoft T 1989 *J. Phys.: Condens. Matter* **1** 6105
[11] Plumer M L and Caillé A 1988 *Phys. Rev.* B **37** 7712
[12] Plumer M L 1984 *PhD Thesis* University of Toronto
[13] Lundgren L, Beckman O, Attia V, Bhattacherjee S P and Richardson M 1970 *Phys. Scr.* **1** 69
[14] Walker M B 1989 *Phys. Rev.* B **40** 9315
[15] Horner H and Varma C M 1968 *Phys. Rev. Lett.* **20** 845
[16] Hornreich R M and Shtrikman S 1976 *J. Phys. C: Solid State Phys.* **9** L683
[17] Belov K P, Zvezdin A K, Kadomtseva A M and Levitin R Z 1976 *Sov. Phys.–Usp.* **19** 574
[18] Aharony A 1973 *Phys. Rev.* B **8** 4270
[19] Franus-Muir E, Plumer M L and Fawcett E 1984 *J. Phys. C: Solid State Phys.* **17** 1107
[20] Kosterlitz J M, Nelson D R and Fisher M E 1976 *Phys. Rev.* B **13** 412
[21] Plumer M L, Caillé A and Hood K 1989 *Phys. Rev.* B **39** 4489